JOURNAL of
MATERIALS and MECHATRONICS:A

e-ISSN 2717-8811
JournalMM, 2024, 5(1), 195-213
https://doi.org/10.55546/jmm.1498662

Araştırma Makalesi / Research Article

Investigation on Microstructural and Mechanical Properties of $FeNiMnCrCoTi_{0.1}$ High Entropy Alloy with B Addition

Mahmud Cemaleddin YALÇIN[1*], Şükrü TALAŞ[2]

[1*] Afyon Kocatepe University, Faculty of Technology, Department of Metallurgical and Materials Engineering, Afyonkarahisar, Turkey,
ORCID ID: https://orcid.org/0000-0003-1685-7319, mcyalcin@aku.edu.tr
[2] Afyon Kocatepe University, Faculty of Technology, Department of Metallurgical and Materials Engineering, Afyonkarahisar, Turkey,
ORCID ID: https://orcid.org/0000-0002-4721-0844, stalas@aku.edu.tr

Geliş/ Received: 10.06.2024**;** **Revize/Revised:** 25.06.2024 **Kabul / Accepted:** 25.06.2024

ABSTRACT: High-entropy alloys (HEAs) are alloys with high potential for use in defense, aircraft, and aerospace industries due to their properties such as high strength, hardness, wear resistance, corrosion resistance, and ability to operate at high temperatures. Therefore, in this study, $FeNiMnCrCoTi_{0.1}B_X$ (x values in molar ratio, x = 0-1) high entropy alloys were produced by arc melting technique under protective gas atmosphere using a reverse vacuum method. The microstructural properties of the produced HEAs were examined by scanning electron microscopy (SEM), and energy-dispersive X-ray spectroscopy (EDX) analysis was also performed. The crystal lattice structure of the produced HEAs was determined by X-ray diffraction (XRD) analysis. Microhardness and compression tests were conducted to determine the mechanical properties of the produced HEAs. It is observed that the hardness of the $FeNiMnCrCoTi_{0.1}B_X$ high-entropy alloy increases as the boron content increases. The highest microhardness obtained was 593.8 HV in the $FeNiMnCrCoTi_{0.1}B$ alloy. As the boron content increases, the yield stress has also increased in compression testing. The highest yield stress was determined to be 1329 MPa in the $FeNiMnCrCoTi_{0.1}B$ alloy.

Keywords: High Entropy Alloy, Arc Melting, Microhardness, Compression Test, Physical Properties.

*Sorumlu yazar / Corresponding author: mcyalcin@aku.edu.tr
Bu makaleye atıf yapmak için /To cite this article

Yalçın, M.C., Talaş, Ş. (2024). Investigation of Microstructural and Mechanical Properties of $FeNiMnCrCoTi_{0.1}$ High Entropy Alloy with B Addition. Journal of Materials and Mechatronics: A (JournalMM), 5(1), 195-213.

1. INTRODUCTION

High-entropy alloys (HEAs), differ from traditional single-element-based alloys (such as Fe, Cu, Ni, Al, Mg, and Ti, etc.) in that they consist of at least 5 principal elements in equimolar or near-equimolar proportions in their structure, rather than having a single primary element matrix (Yeh et al., 2004; Zhang et al., 2018). These alloys, due to their high mixture entropy, tend to be more stable and often form solid solutions containing complex phases instead of simple ones, including both face-centered cubic (FCC) and body-centered cubic (BCC) crystal structures (Zhou et al., 2007; Yang and Zhang, 2012). In 2006, Yeh (Yeh, 2006) described high-entropy alloys, explaining that the combination of multiple principal elements leads to high entropy, lattice distortion, slow diffusion, and cocktail effects (Yeh, 2006; İçin et al., 2023).

High-entropy alloys, due to their ability to combine superior properties such as high strength, high wear resistance, stability at high temperatures, good corrosion resistance, have broad application potential in various sectors including defense, aerospace, nuclear, automotive industry, superconductors, and healthcare (Zhang et al., 2014; Gao et al., 2018; Murty et al., 2014). Various methods are used to produce HEAs, including mechanical alloying-sintering (solid-state), magnetron sputtering (physical vapor deposition), selective laser melting (additive manufacturing), induction melting (liquid state), and vacuum arc melting (liquid state). Among these, vacuum arc melting is the most commonly used method (Murty et al., 2014; Algan Şimşek et al., 2022). In this method, all elements are melted into a liquid state inside a copper crucible in an inert gas environment by an arc formed by a tungsten electrode tip and then solidified in the copper crucible. To ensure the chemical homogeneity of the alloys, multiple melting and solidification cycles are often performed. The shape of the solidified samples is button-shaped inside a cup-like copper crucible. To facilitate sample preparation processes for analyses such as tension and compression, the button-shaped sample is poured into a pre-machined cylindrical copper mold (Zhou et al., 2007; Gao et al., 2016).

The effects of elemental additions made to high-entropy alloys on the crystal structure and microstructure morphology have been observed to have positive impacts on mechanical properties in many studies (He et al., 2014). The FeNiMnCrCo high-entropy alloy exhibits approximate yield strength of 200 MPa and approximate ultimate tensile strength of 600 MPa at room temperature, depending on grain size (Otto et al., 2013). Due to its relatively low strength, numerous studies have been conducted to establish a good balance between strength and ductility. This alloy possesses excellent work hardening ability, exceptional ductility at both room and cryogenic temperatures, and promising fracture toughness at cryogenic temperatures. These properties make these alloys attractive for industrial applications and encourage researchers to explore the addition of intermediate elements (Shahmir et al., 2023).

In the studies of $Al_{0.5}$CoCrCuFeNiTix (Chen et al., 2006) and CoCrFeNiTix (Shun et al., 2012), it has been observed that the addition of Ti improves the mechanical properties. This observation is attributed to the altered crystal structure due to the addition, and these alloys have either a BCC or a FCC crystal structure, or a mixture of both. Generally, alloys with a body-centered cubic crystal structure exhibit higher strength compared to alloys with a face-centered cubic crystal structure, but they are more difficult to process (Chuang et al., 2011). In the study conducted by Algan Şimşek and colleagues (Algan Şimşek et al., 2021), it is observed that the addition of boron to the FeNiCoCrCu high-entropy alloy has a positive effect on the mechanical properties. Similarly, in the research conducted by Xiaotao and colleagues (Xiaotao et al., 2016), it is observed that boron addition to the $Al_{0.5}$CoCrCuFeNi high-entropy alloy contributes positively to the mechanical properties. Taking all

of these into consideration, we investigated the microstructure and mechanical properties of the $FeNiMnCrCoTi_{0.1}$ high-entropy alloy with the addition of B.

2. MATERIALS AND METHODS

The flowchart of processes employed in this study is provided in Figure 1 and was followed to ensure the experimental activities conducted effectively.

Figure 1. Flowchart of the experimental study

In order to create $FeNiMnCrCoTi_{0.1}Bx$ (x values in molar ratio, x= 0-1) high-entropy alloys, Ni, Mn, Cr, Co, and B powders from Nanografi company with a purity of 99.9% and Fe and Ti granules from Alfa Aesar company with a purity of 99.9% were obtained as raw materials, each with a particle size of 325 mesh.

The general properties of the powders used for alloy making and the alloy composition and are given in Table 1 and Table 2, respectively.

Table 1. General properties of the powders used for alloy making

Material	Commercial References	Molecular Weight (g/mol)	Purity (%)	Density (g/cm^3)	Melting Point (°C)	Boiling Point (°C)
Fe	Alfa Aesar	55.845	99.98	7.8	1535	3000
Ni	Nanografi	58.693	99.99	8.9	1453	2730
Mn	Nanografi	54.938	99.99	7.43	1245	2150
Cr	Nanografi	51.996	99.99	7.19	1857	2672
Co	Nanografi	58.933	99.99	8.92	1495	2900
Ti	Alfa Aesar	47.867	99.99	4.5	1668	3260
B	Nanografi	10.811	99	2.34	2300	2550
Mo	Nanografi	95.95	99.95	10.2	2610	5560

Table 2. . The nominal composition of alloys made in this study based on $FeNiMnCrCoTi_{0.1}B_X$

HEA		Ratio of Elements							Total
		Fe	Ni	Mn	Cr	Co	Ti	B	
$FeNiMnCrCoTi_{0.1}$	R (%)	19.61	19.61	19.61	19.61	19.61	1.96	-	100
$FeNiMnCrCoTi_{0.1}B_{0.2}$	R (%)	18.87	18.87	18.87	18.87	18.87	1.89	3.77	100
$FeNiMnCrCoTi_{0.1}B_{0.4}$	R (%)	18.18	18.18	18.18	18.18	18.18	1.82	7.27	100
$FeNiMnCrCoTi_{0.1}B_{0.6}$	R (%)	17.54	17.54	17.54	17.54	17.54	1.75	10.53	100
$FeNiMnCrCoTi_{0.1}B_{0.8}$	R (%)	16.95	16.95	16.95	16.95	16.95	1.69	13.56	100
$FeNiMnCrCoTi_{0.1}B$	R (%)	16.39	16.39	16.39	16.39	16.39	1.64	16.39	100

The molar weights of the elements were calculated and then weighed using high sensitivity Dikomsan ES410D balance. The weighed powders were mixed for half an hour, and then pressed uniaxially at 250 MPa pressure using 60 ton press (Figure 2 a) in a cylindrical mold with a diameter of 20 mm (Figure 2 b).

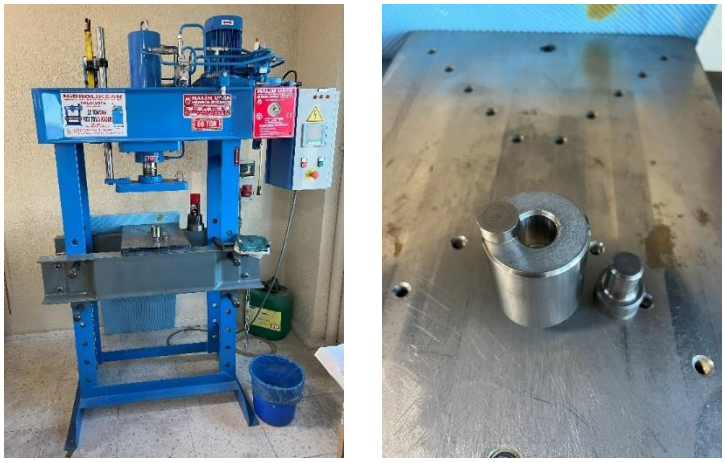

(a) (b)

Figure 2. a) uniaxial press machine b) 20 mm diameter steel mold

For the melting process, the pressed sample was placed in a copper crucible, and melting was performed using a Nuriş DC-TIG/ARC350 welding machine equipped with a tungsten electrode tip, applying a current of 300 Amperes (A) while purging argon onto the sample. To ensure chemical homogeneity, samples were melted four times. Additionally, after each melting, the surface impurities were cleaned by brushing with a wire brush, and then the samples were remelted by turning them upside down.

After the melting process, the samples were poured into a 6 mm diameter copper mold using the reverse vacuum method with a current of 300 A to give them a cylindrical shape. These processes are shown in Figure 3 (a) and (b).

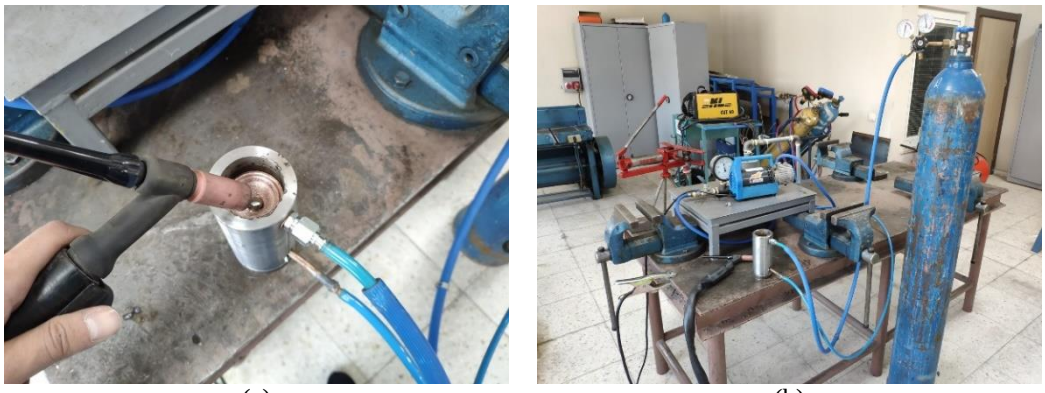

(a) (b)

Figure 3. a) Copper casting mold, b) reverse vacuum casting system

The cylindrical samples obtained after casting were machined on a lathe to flatten their outer surfaces. Subsequently, the machined samples were cut using a precision cutting machine. The cut samples were then reattached to the lathe and sanded with 120, 240, 400, 600, 800, 1000, and 1200 G SiC sandpapers to make the top and bottom surfaces completely parallel. Then, XRD scans were performed using a Bruker D8 Advance X-ray diffractometer with Cu-Kα (λ= 1.542 Å) radiation source in the range of 2θ=20-100°, and XRD peaks were analyzed. Next, the samples were polished using velvet cloth with 1µm alumina (Al_2O_3) suspension in FORCIPOL 2V device for hardness testing and microstructure examination. After polishing, the samples were etched with aqua regia, and their microstructures were examined using a LEO 1430 VP SEM with a backscattered electron detector, and semi-quantitative elemental analysis was performed using an EDX detector. Finally, for the determination of mechanical properties, Vickers microhardness tests were conducted using the MICROBUL microhardness measurement device with a 100g load applied for 10 seconds at 10 different points, and compression tests were performed using the MICROANALIZ UNIVERSAL TEST MACHINE 100kN device.

3. RESULTS AND DISCUSSION

XRD pattern of the $FeNiMnCrCoTi_{0.1}B_X$ high-entropy alloy is given in Figure 4. Upon examination of the XRD pattern, it is observed that $FeNiMnCrCoTi_{0.1}$ exhibits a single-phase FCC crystal structure, and as the addition of B increases, the presence of the FCC crystal structure is maintained. In a study conducted by Mehranpour et al., it is observed that the homogenized $FeNiMnCrCoTi_{0.1}$ alloy exhibits a single-phase FCC crystal structure (Mehranpour et al., 2021). Peaks corresponding to borides were detected, although with very low intensity, in the study conducted by Xiaotao and colleagues (Xiaotao et al., 2016). Similarly, in our XRD analyses, low-intensity peaks resembling borides are also observed.

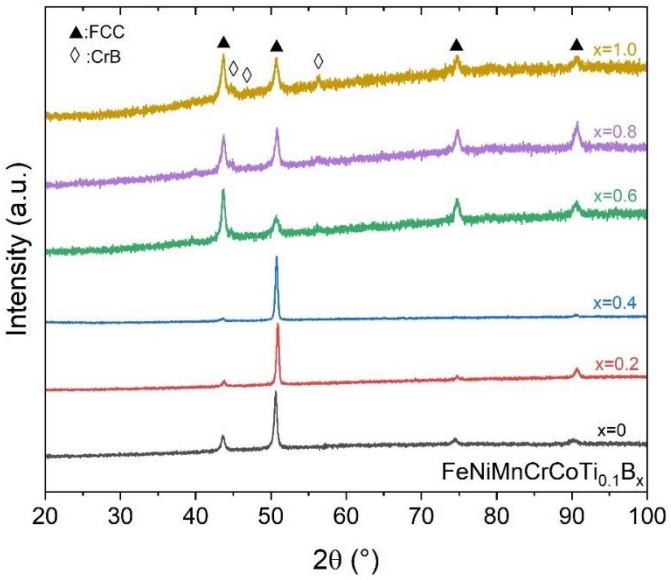

Figure 4. X-ray diffraction patterns of $FeNiMnCrCoTi_{0.1}B_X$ alloys

In Figure 5, the results of microstructural analysis using a SEM with a backscattered electron detector and semi-quantitative elemental analysis using an EDX detector are shown. In the high-magnification EDX point analysis seen in Figure 5 (a-1), it is observed that a segregation with high amount of Ti occurs within the grains or along the phase boundaries. This situation is also observed in the study conducted by İçin (İçin, 2024). In the EDX point analysis in Figure 5 (a-2), it is clearly observed that the matrix is in the form of solid solution of FCC phase (Otto et al., 2016) and contains Cr, Mn, Fe, Co, and Ni in similar proportions. Similar situations are observed in other EDX analyses with boron additions. However, the same study by Otto et.al (Otto et al., 2016) also showed that mainly FCC and in addition many minor phases formed after melting that are FCC + Cr-rich BCC + Ni-Mn rich L10 + Fe-Co rich B2, which were not clearly observed in this study as the specimens in this study was not heat treated following the casting or fell below the detection limit of XRD analysis. Nevertheless, this study was carried out without the addition of Ti and B, which may have had little effect on the matrix solid solution phase but rather may be effective in the formation of precipitation, for example, Ti addition introduces A_3B, A_2B and/or A_2BC (Laves) types of precipitation into the matrix (Chuang et al., 2011; Luan et al., 2019), increasing the matrix hardness significantly. As the amount of Boron addition increases, as was shown in the study by Xiaotao and colleagues (Xiaotao et al., 2016), needle-like boride precipitates were observed. This structure is located beneath the Ti segregation, as seen in Figure 5 (b-1), hence the Ti ratio appears to be lower in atomic ratio in the EDX analysis. Considering XRD and EDX analyses, the likelihood of needle-like precipitates being CrB is very high. As the boron addition increases, it is observed that the needle-like precipitates also increase in size and amount.

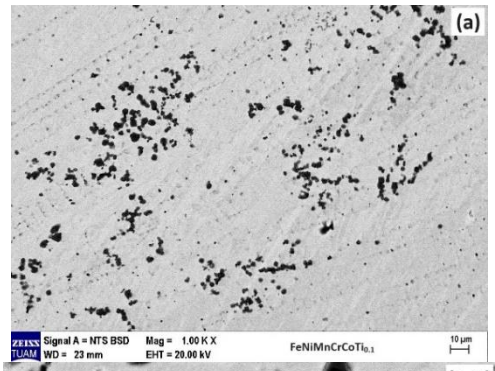

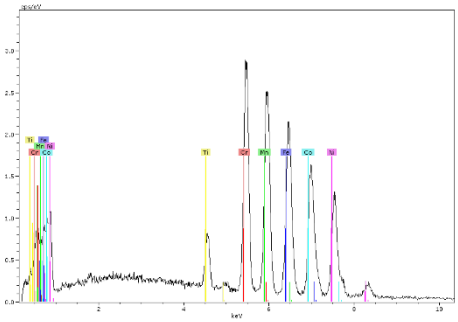

Element	Atomic (%)
Ti	2.89
Cr	21.71
Mn	19.24
Fe	20.48
Co	18.61
Ni	17.07

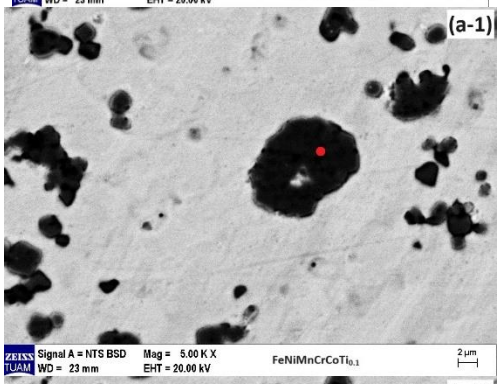

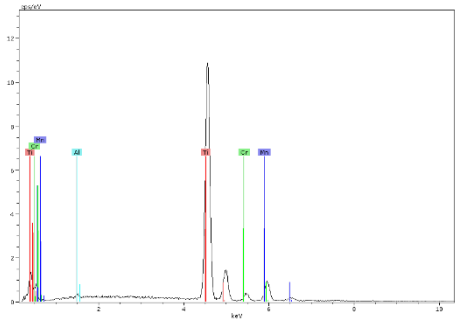

Element	Atomic (%)
Ti	85.39
Cr	4.13
Mn	10.48

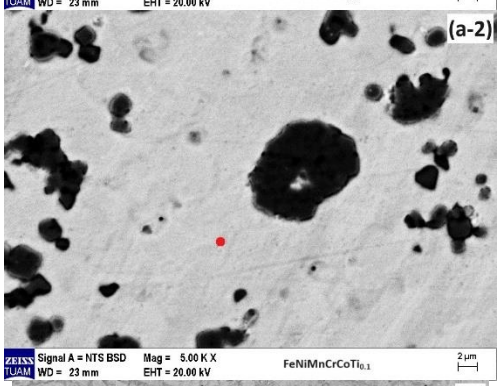

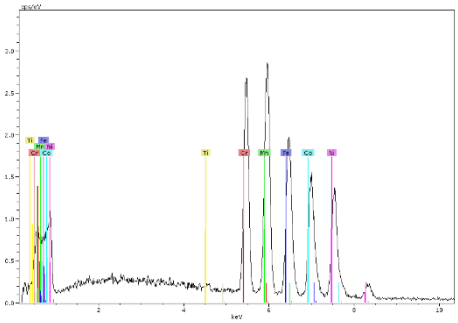

Element	Atomic (%)
Ti	0
Cr	21.25
Mn	22.81
Fe	18.52
Co	18.57
Ni	18.85

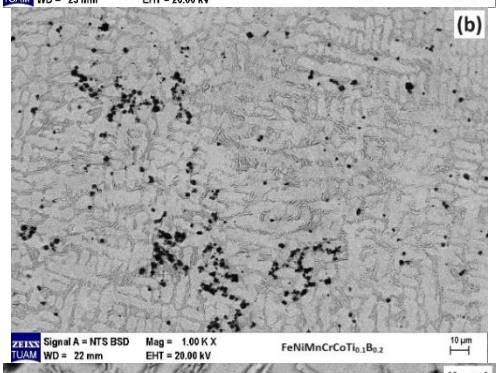

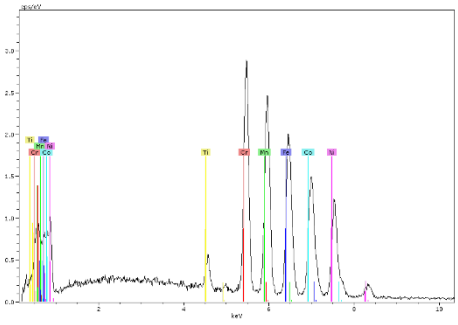

Element	Atomic (%)
Ti	1.45
Cr	23.04
Mn	19.11
Fe	20.48
Co	19.19
Ni	16.74

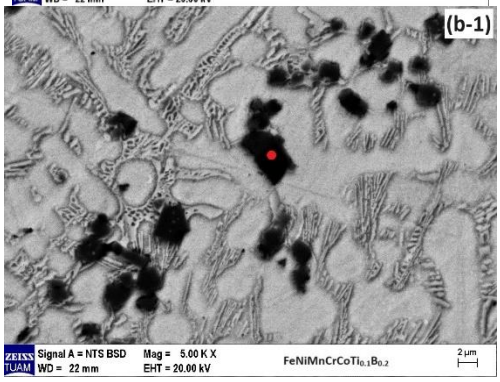

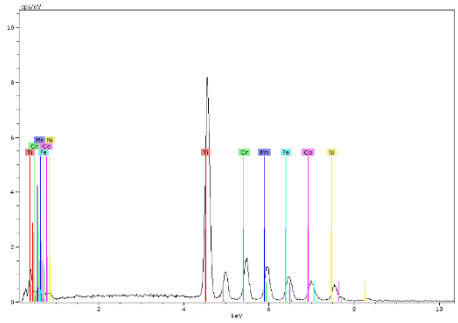

Element	Atomic (%)
Ti	49.29
Cr	13.86
Mn	10.70
Fe	9.70
Co	8.99
Ni	7.47

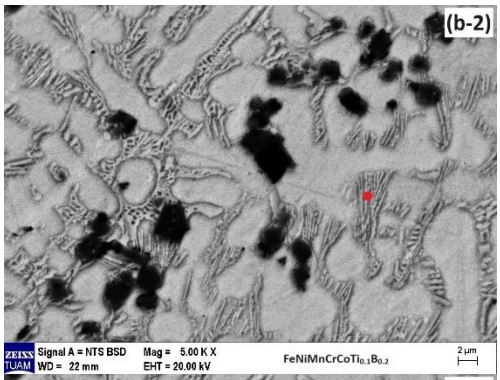

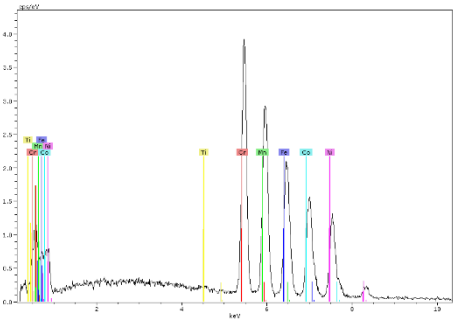

Element	Atomic (%)
Ti	0
Cr	27.73
Mn	20.29
Fe	18.82
Co	17.65
Ni	15.51

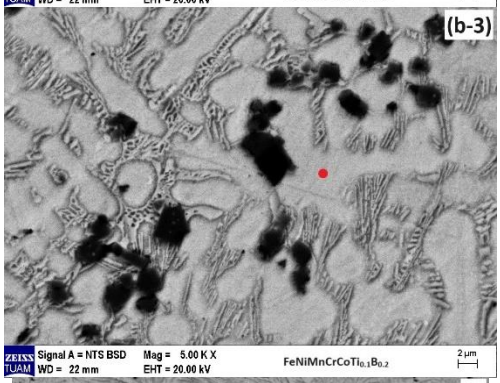

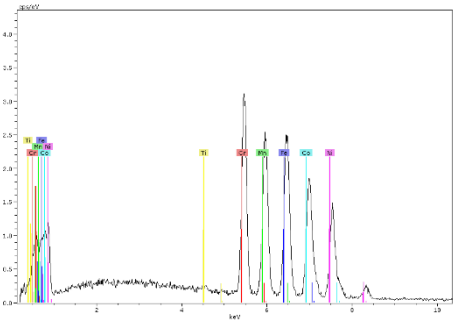

Element	Atomic (%)
Ti	0
Cr	21.55
Mn	16.97
Fe	24.07
Co	20.06
Ni	17.35

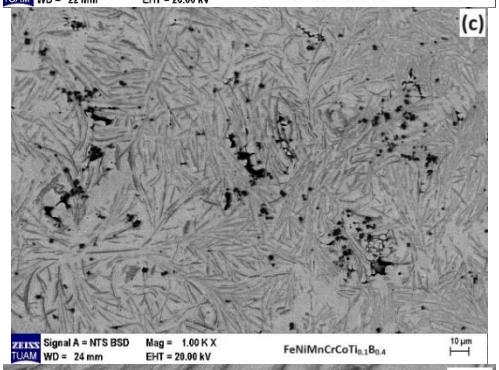

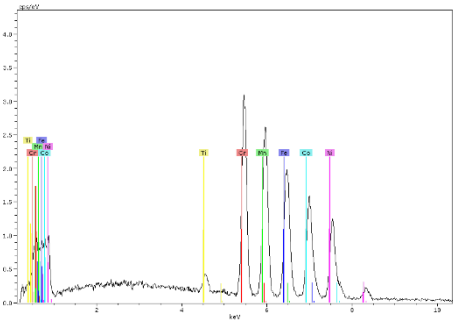

Element	Atomic (%)
Ti	0,76
Cr	23.99
Mn	19.42
Fe	19.84
Co	19.13
Ni	16.86

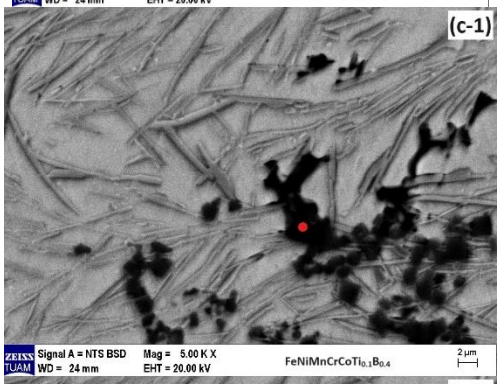

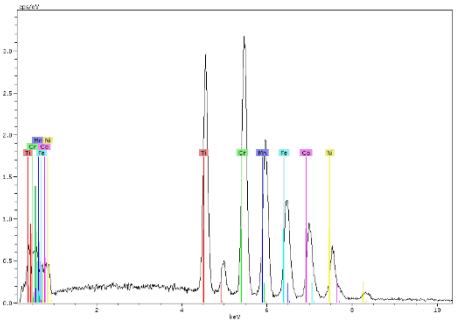

Element	Atomic (%)
Ti	18.10
Cr	31.38
Mn	14.88
Fe	14.45
Co	12.02
Ni	9.16

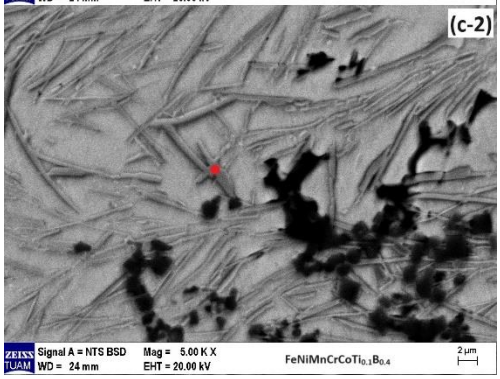

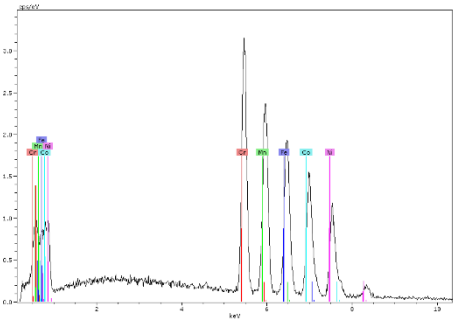

Element	Atomic (%)
Ti	0
Cr	26.00
Mn	18.58
Fe	20.54
Co	19.01
Ni	15.86

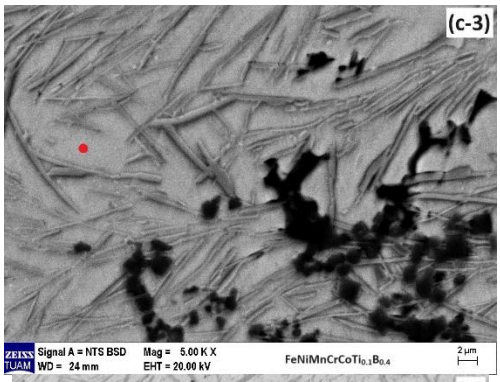

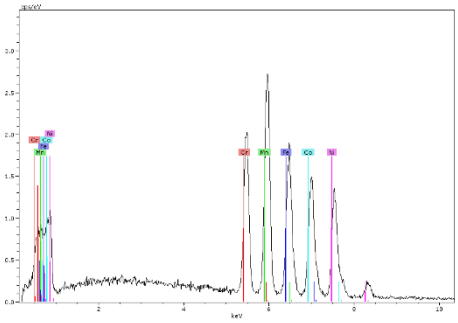

Element	Atomic (%)
Ti	0
Cr	18.17
Mn	24.32
Fe	17.38
Co	21.05
Ni	19.07

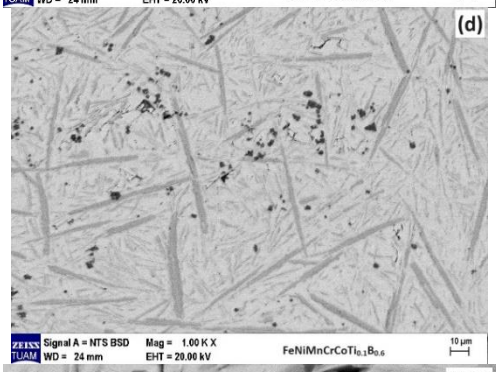

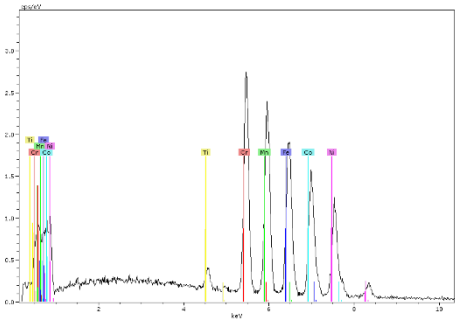

Element	Atomic (%)
Ti	0.90
Cr	23.31
Mn	19.18
Fe	20.59
Co	19.20
Ni	16.83

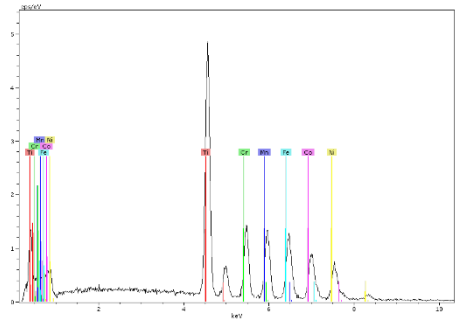

Element	Atomic (%)
Ti	33.80
Cr	14.23
Mn	13.17
Fe	15.12
Co	12.83
Ni	10.84

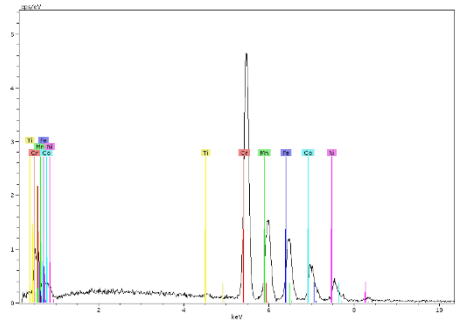

Element	Atomic (%)
Ti	0
Cr	55.24
Mn	10.13
Fe	18.15
Co	10.60
Ni	5.88

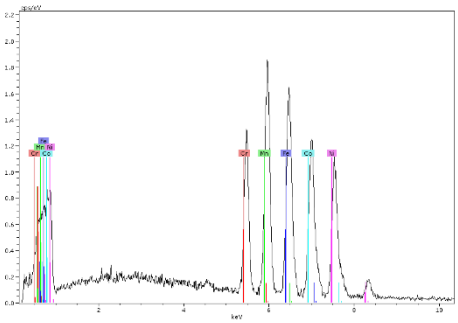

Element	Atomic (%)
Ti	0
Cr	13.11
Mn	21.65
Fe	22.42
Co	21.78
Ni	21.05

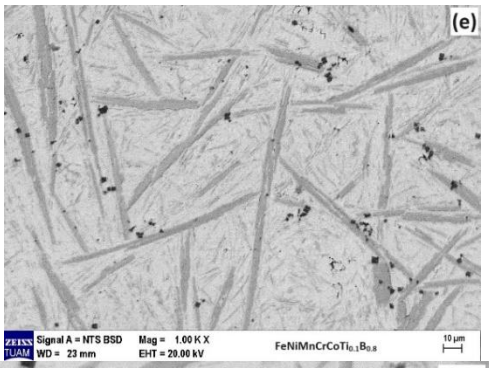

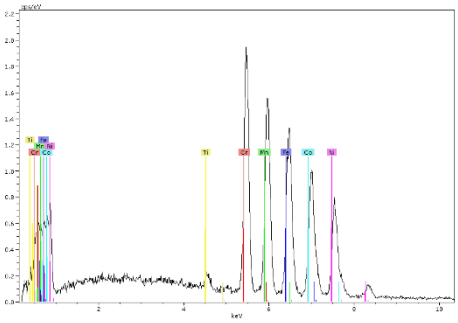

Element	Atomic (%)
Ti	0.29
Cr	24.19
Mn	18.54
Fe	21.68
Co	19.30
Ni	15.98

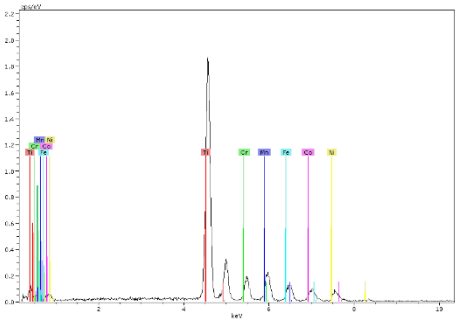

Element	Atomic (%)
Ti	62.41
Cr	9.71
Mn	10.36
Fe	6.72
Co	6.42
Ni	4.37

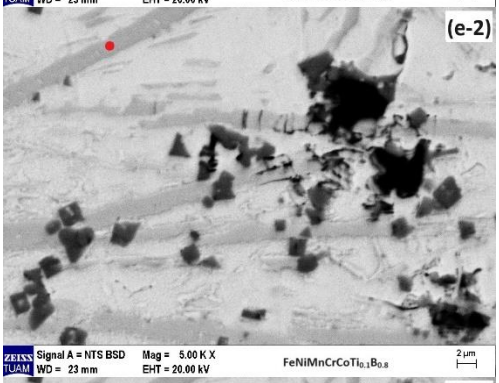

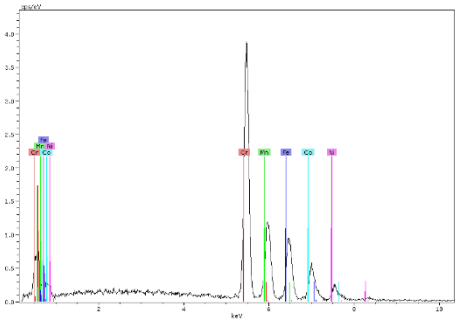

Element	Atomic (%)
Ti	0
Cr	55,72
Mn	10.92
Fe	18.99
Co	9.71
Ni	4.65

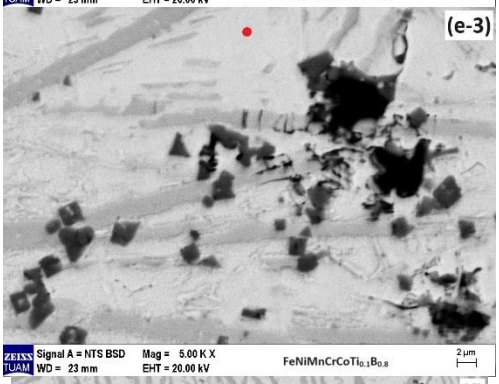

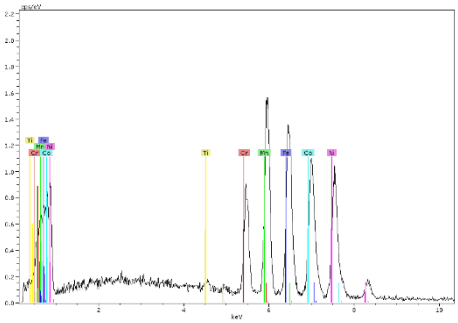

Element	Atomic (%)
Ti	0.05
Cr	10.05
Mn	22.28
Fe	22.23
Co	22.74
Ni	22.55

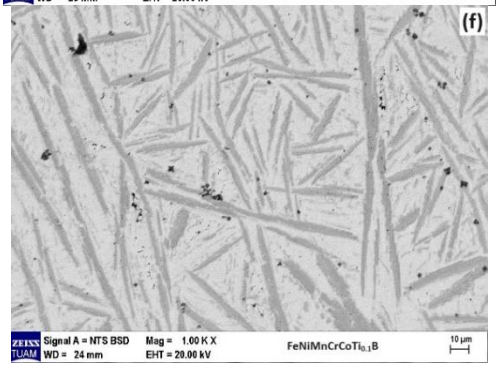

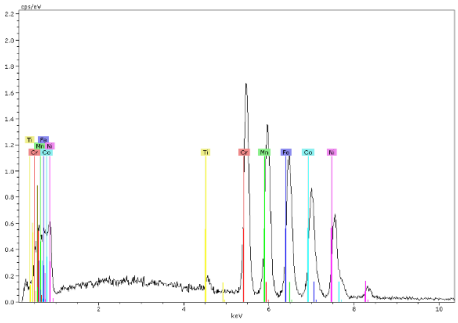

Element	Atomic (%)
Ti	0.15
Cr	24.59
Mn	19.06
Fe	20.76
Co	19.69
Ni	15.74

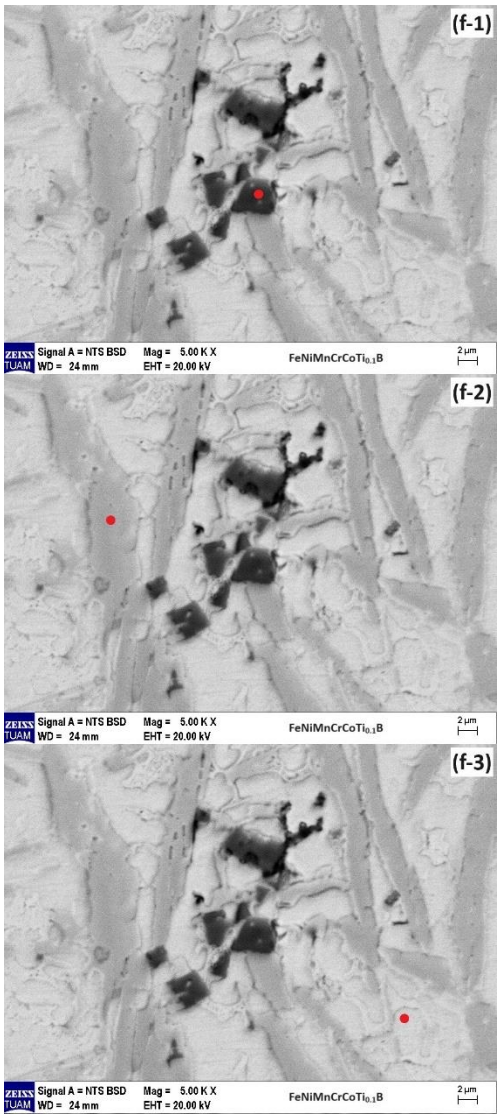

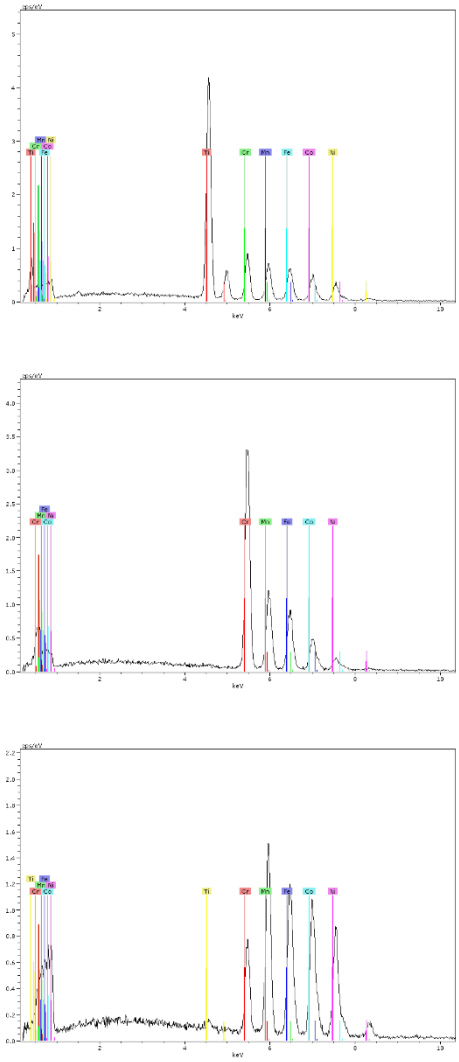

Element	Atomic (%)
Ti	46.10
Cr	14.63
Mn	9.76
Fe	12.06
Co	9.88
Ni	7.56

Element	Atomic (%)
Ti	0
Cr	54.99
Mn	11.42
Fe	19.61
Co	9.76
Ni	4.22

Element	Atomic (%)
Ti	0.20
Cr	9.59
Mn	24.33
Fe	21.30
Co	23.88
Ni	20.70

Figure 5. SEM images and EDX spectra of $FeNiMnCrCoTi_{0.1}B_X$ alloys with various boron (a) x:0 (b) x:0.2 (c) x:0.4 (d) x:0.6 (e) x:0.8 and (f) x:1 mol

As seen in Figure 6, the hardness of the $FeNiMnCrCoTi_{0.1}$ high-entropy alloy was measured to be 200.4 HV as the average of ten measurements. As the ratio of boron addition increases, the hardness of the alloy also increases significantly. In Figure 5(d-f), the average number of needles per 5cmx5cm square appears to be 126 (x: 0.4), 36 (x: 0.6), 31 (x: 0.8) and 29 (x: 1), respectively. However, the aspect ratios of needles are 0.33, 0.28, 0.21 and 0.11, respectively. These results indicate that as the amount of boron increases the needle becomes less in number but elongates and few number of needles become thicker in width. As the number of needles is high in the first series of boron addition, it significantly becomes thick and number decreases in later additions.

The highest hardness value, with an average of ten measurements, was achieved in the $FeNiMnCrCoTi_{0.1}B$ alloy, measuring 593.8 HV. With the addition of boron, the amount of needle-like structures increases and they become elongated in shape and net like appearance of these needle like structures are believed to be increasing the overall hardness of the specimens as shown in Figure 6. As seen Figure 5(e) that it is likely that (Cr, Fe)B constitutes the needle like structures which was also suggested by Xiaotao et al (Xiaotao et al., 2016). It is interesting to note that as seen in Figure 5(b) the needle like phase separation was observed as a eutectic phase separation which suggest that this zone is gradually becoming rich in eutectic making elements however, the EDX analysis was

not able to detect the boron content. A seaweed appearance of second phase in high entropy alloys was observed in FeNiCoCrMnPd eutectic high entropy alloys in addition to FCC+ Mn_7Pd_9 precipitates (Tan et al., 2017); with the addition of Nb into FeNiCrCoMn i.e. FeNiCrCoMnNb (Huo et al., 2015), the phase separation concludes as FCC+laves phase (A_2B or A_2BC) and the appearance becomes lamellar as shown in Figure 5(c). However, the excessive addition of boron transforms seaweed appearance into initially to lamellar and then the appearance becomes needle like and/or lamellar. The addition of Ti also produces the same effect as lamellar structure in addition to FCC+laves phase (Jain et al., 2018). It can be suggested that at the composition of $FeNiMnCrCoTi_{0.1}B_{0.2}$ the alloy shows eutectic high entropy alloy behavior and can be regarded as one.

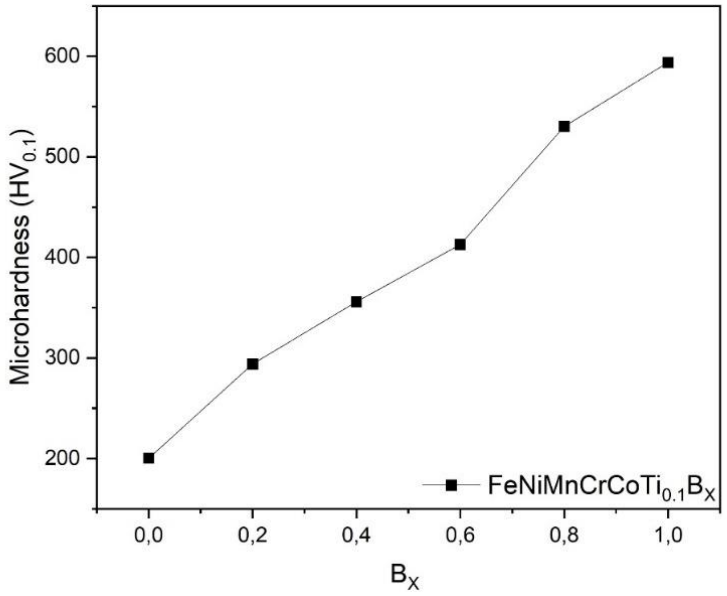

Figure 6. Hardness graph of $FeNiMnCrCoTi_{0.1}B_X$ alloys

In Figure 7, the stress-strain curve of the $FeNiMnCrCoTi_{0.1}B_X$ compression test conducted at room temperature is depicted. As observed in the stack of curves, with the increase in boron addition, the strain percentage decreases significantly for the first two specimens, however, for boron addition of x: 0.4 - x: 1, the strain is less pronounced. Nevertheless, regardless of strain increase rate, yield stress gradually increases and becomes stable after x: 0.4 addition of boron.

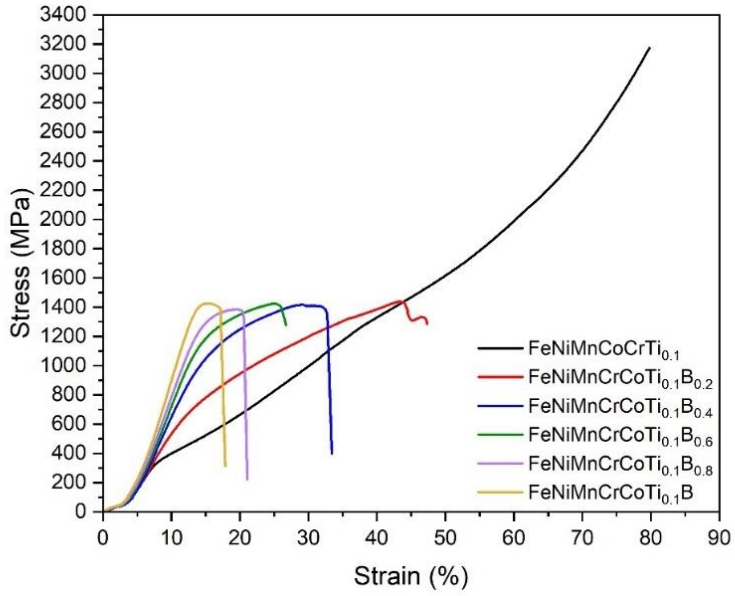

Figure 7. Room-temperature compression stress-strain curves of $FeNiMnCrCoTi_{0.1}B_X$ alloys

In Figure 8, the yield stress graph varying with boron content is shown. As depicted in the graph, the yield stress of the $FeNiMnCrCoTi_{0.1}$ high-entropy alloy is 329 MPa. With increasing boron addition, a gradual increase in the yield stress was observed, which was believed to be due to increasing amount of needle like structures. The highest yield stress, reaching 1329 MPa, was obtained in the $FeNiMnCrCoTi_{0.1}B$ alloy. As was stated that the aspect ratio of needles were proved to be decreasing i.e. becomes elongated with respect to increasing addition of boron. This implies that strength is more affected not by the number of needles but more to do with length of the needles i.e. aspect ratio, as it will affect the deformation capacity if there are larger precipitates and crack formation and advancement are hindered in these specimens.

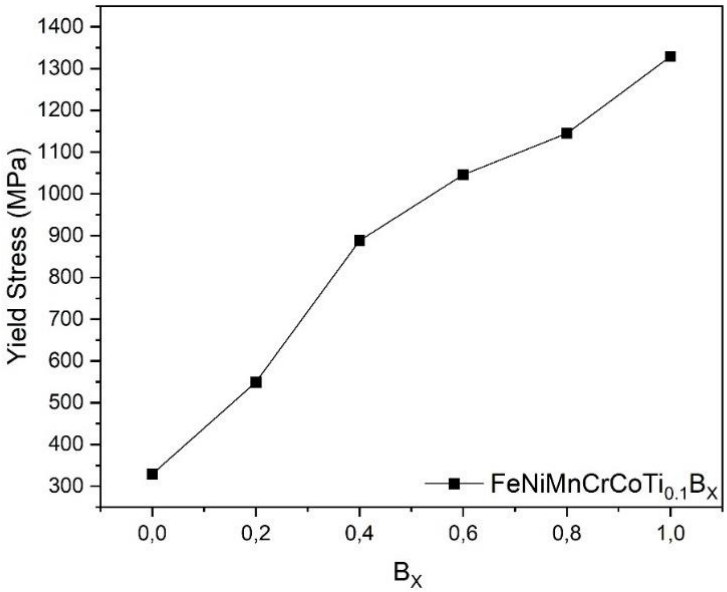

Figure 8. Compression 0.2% offset yield stress graph of $FeNiMnCrCoTi_{0.1}B_X$ alloys

In Figure 9, the maximum compression stress graph varying with boron content is depicted. The maximum compression stress value of the $FeNiMnCrCoTi_{0.1}$ high-entropy alloy is 3167 MPa.

This value was obtained with an applied load of 80 kN, which is the capacity of the compression test machine, and the sample remained unbroken. Depending on the boron addition, the maximum compression stress varies between 1384 MPa and 1438 MPa. The highest compression stress, reaching 1438 MPa, was achieved in the FeNiMnCrCoTi0.1$B_{0.2}$ alloy. However, the aspect ratio of needles have little effect on the maximum compression strength as it may indicate that the matrix phase in addition to the distribution is also a dominant factor in obtaining a high compression rate.

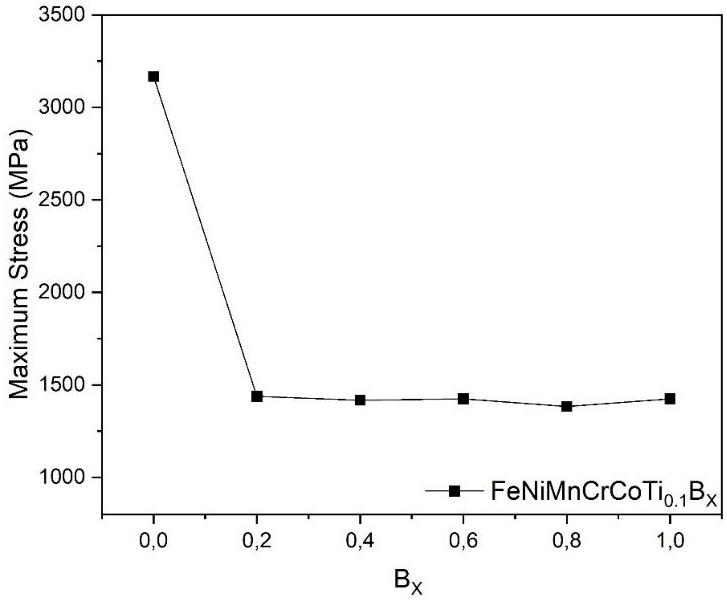

Figure 9. Compression maximum stress graph of FeNiMnCrCoTi$_{0.1}B_X$ alloys

In Figure 10, the percentage elongation graph varying until fracture with respect to boron content is shown. The highest percentage elongation was measured as 79.73% in the FeNiMnCrCoTi$_{0.1}$ high-entropy alloy. The lowest percentage elongation was measured as 17.85% in the FeNiMnCrCoTi$_{0.1}$B alloy. The microstructures given in Figure 9(a and b) is suitable for the defition of bimodal microstructures that is two different morphology exists at the same time where the microstructures given in Figure 5(c-f) are compatible with the definition of bilamellar structures. As the amount of boron increases, similar to hardness variation curves, the strain at maximum compression strength drops dramatically as the the needle morphology transforms from high in number and smaller in size to low in number but elongated in shape form. The deformation capacity of alloys with higher boron content may be affected by thick phase boundaries through which a crack cannot pass whereas thinner sections of needles can easily be broken by the action of crack (propagation) or passed by dislocation movement. It was shown that bilamellar structure is more effective in diverting the crack propagation than bimodal microstructures (Tan et al., 2021; Tan et al., 2017). The apperance of crack features also align with this view because of their height at which the crack occurred.

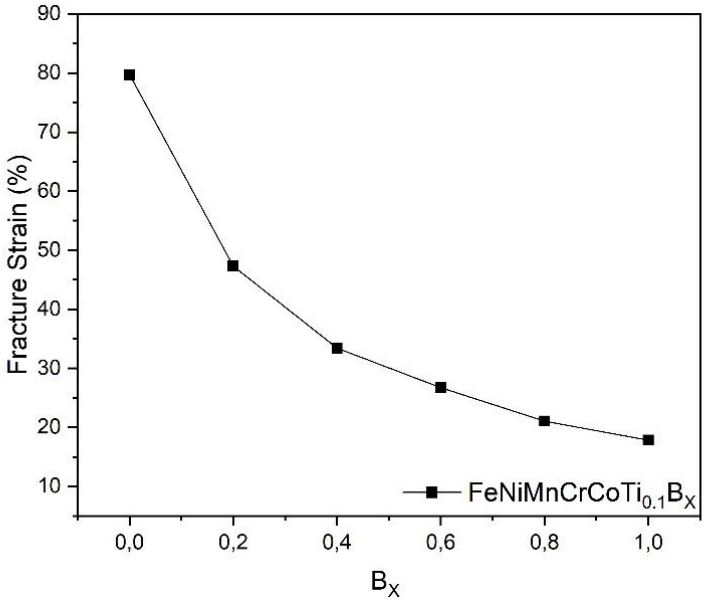

Figure 10. Compression fracture strain graph of $FeNiMnCrCoTi_{0.1}B_X$ alloys

In Figure 11, sample images before and after the compression test are provided. With increasing boron content, the height of compression specimen did not decrease, that is, compared to specimens with boron content of x: 0, x: 0.2, x: 0.4 (Figure 11 (b, d and f)), the specimens shown in Figure 11 (h, I and j) were not affected by the compression force in height. This can also be observed in Table 3, showing the mechanicla properties of alloys tested in this study with respect to their boron additions.

Table 3. Mechanical properties of $FeNiMnCrCoTi_{0.1}B_X$ at room temperature**.**

Alloys	$\sigma_{0.2}$ (MPa)	σ_{max} (MPa)	ε_f (%)	HV
$FeNiMnCrCoTi_{0.1}$	329	--	79.73	200.4
$FeNiMnCrCoTi_{0.1}B_{0.2}$	549	1438	47.33	293.9
$FeNiMnCrCoTi_{0.1}B_{0.4}$	888	1417	33.42	355.8
$FeNiMnCrCoTi_{0.1}B_{0.6}$	1046	1424	26.71	412.8
$FeNiMnCrCoTi_{0.1}B_{0.8}$	1145	1384	21.05	530.1
$FeNiMnCrCoTi_{0.1}B$	1329	1425	17.85	593.8

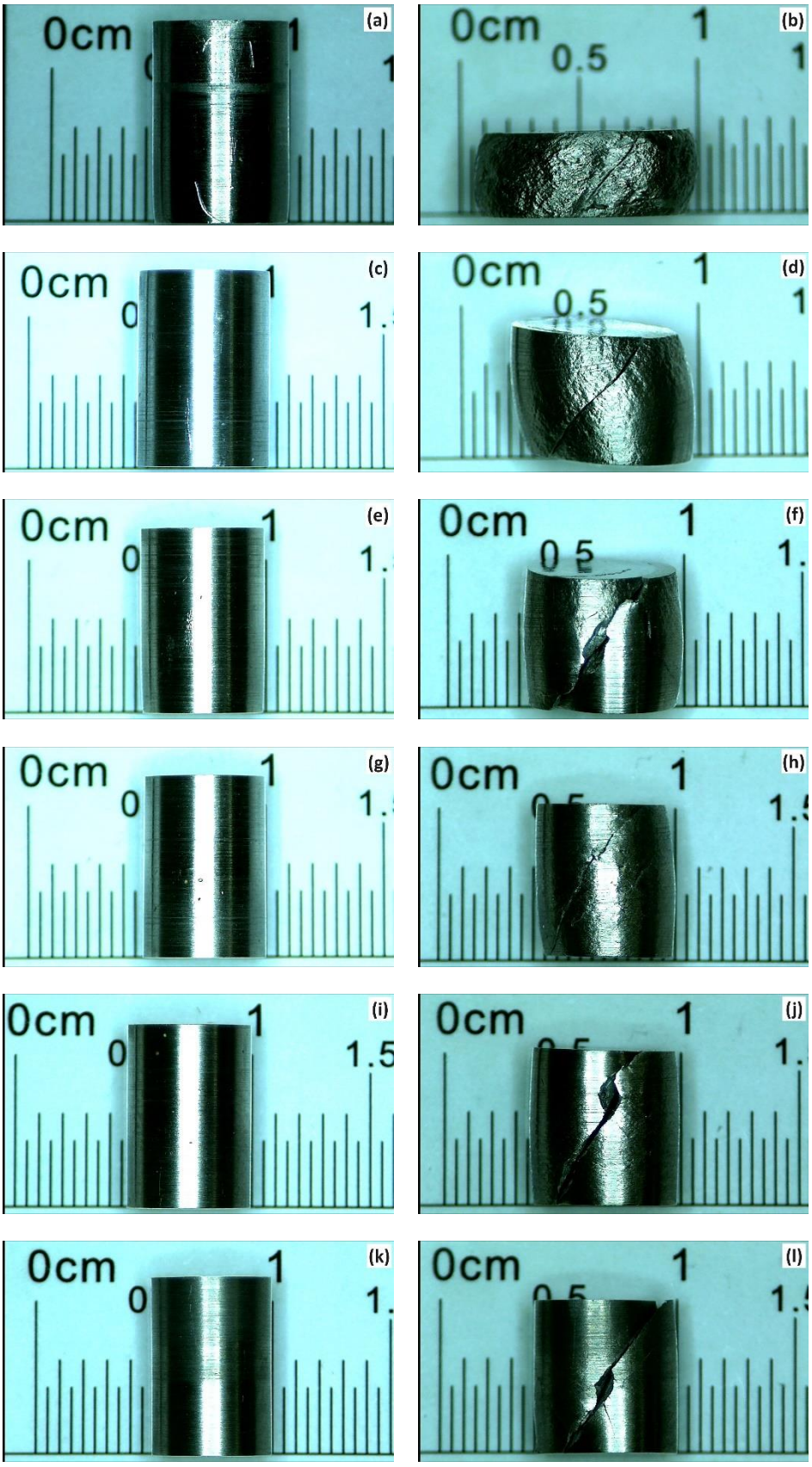

Figure 11. Before (a, c, e, g, i, k) and after (b, d, f, h, j, l) compression test sample images of $FeNiMnCrCoTi_{0.1}B_X$ alloys

4. CONCLUSION

The results obtained by adding B to the $FeNiMnCrCoTi_{0.1}$ high-entropy alloy are provided below.

- Despite the arc melting process being conducted with argon blowing in an open atmosphere, no oxide or nitride compounds were observed in the XRD analysis results. This condition is more favorable for industrial production in terms of process feasibility compared to vacuum arc melting.
- Considering the SEM and EDX analysis results, segregation of Ti element was observed, and concurrently, with the increase in boron addition, needle-like CrB precipitates were observed, taking into account of the XRD results.
- Microhardness tests showed that the hardness of the alloy increased with the increase in boron content.
- Compression tests revealed that the yield stress increased with the increase in boron content, while the percentage elongation decreased.

5. ACKNOWLEDGEMENTS

This study was supported by Afyon Kocatepe University Scientific Research Projects Coordination Unit with Project number of 21.FEN.BİL.11.

6. CONFLICT OF INTEREST

Authors approve that to the best of their knowledge, there is not any conflict of interest or common interest with an institution/organization or a person that may affect the review process of the paper.

7. AUTHOR CONTRIBUTION

Both Mahmud Cemaleddin YALÇIN and Şükrü TALAS contributed to determining the concept and/or design process of the research, managing the concept and/or design process of the research, analyzing data and interpreting the results, preparing the manuscript, critically analyzing the intellectual content, and providing final approval and full responsibility. Additionally, Mahmud Cemaleddin YALÇIN also contributed to data collection.

8. REFERENCES

Algan Şimşek İ., Talaş S., Kurt, A., The evolution of phases in FeNiCoCrCuBx high entropy alloys produced through microwave sintering and vacuum arc melting. Revista de Metalurgia, 58(1), 2022.

Algan Şimşek İ.B., Arık M.N., Talaş Ş., Kurt A., The effect of B addition on the microstructural and mechanical properties of FeNiCoCrCu high entropy alloys. Metallurgical and Materials Transactions A, 52, 1749-1758, 2021.

Chen M.R., Lin S.J., Yeh J.W., Chen S.K., Huang Y.S., Tu C.P., Microstructure and properties of Al0. 5CoCrCuFeNiTix (x= 0–2.0) high-entropy alloys. Materials transactions, 47(5), 1395-1401, 2006.

Chuang M.H., Tsai M.H., Wang W.R., Lin S.J., Yeh J.W., Microstructure and wear behavior of AlxCo1. 5CrFeNi1. 5Tiy high-entropy alloys. Acta Materialia, 59(16), 6308-6317, 2011.

Gao M.C., Miracle D.B., Maurice D., Yan X., Zhang Y., Hawk J.A. High-entropy functional materials. Journal of Materials Research, 33(19), 3138-3155, 2018.

Gao M.C., Yeh J.W., Liaw P.K., Zhang Y., High-entropy alloys: fundamentals and applications. Springer. 2016.

He J.Y., Liu W.H., Wang H., Wu Y., Liu X.J., Nieh T.G., Lu Z.P., Effects of Al addition on structural evolution and tensile properties of the FeCoNiCrMn high-entropy alloy system. Acta Materialia, 62, 105-113, 2014.

He J.Y., Wang H., Huang H.L., Xu X.D., Chen, M.W., Wu Y., Liu X.J., Nieh T.G., An K., Lu Z.P., A precipitation-hardened high-entropy alloy with outstanding tensile properties. Acta Materialia, 102, 187-196, 2016.

Huo W.Y., Shi H.F., Ren X., Zhang J.Y., Microstructure and Wear Behavior of CoCrFeMnNbNi High-Entropy Alloy Coating by TIG Cladding. Advances in Materials Science and Engineering, 2015(1), 647351, 2015.

İçin K., Investigation of phase transformation related magnetic properties of Ti addition to FeCoCuNiMn and FeCoCuNiAl high entropy alloys by vacuum arc melting. Materials Today Communications, 39, 108821, 2024.

İçin K., Sünbül S.E., Yıldız A., Cantor Yüksek Entropili Alaşımına Mn Yerine Cu İkamesinin Yapısal ve Mekanik Özellikler Üzerindeki Etkisinin Araştırılması. Gazi University Journal of Science Part C: Design and Technology, 11(2), 379-387, 2023.

Jain R., Rahul M.R., Jain S., Samal S., Kumar V., Phase evolution and mechanical behaviour of Co–Fe–Mn–Ni–Ti eutectic high entropy alloys. Transactions of the Indian Institute of Metals, 71, 2795-2799, 2018.

Luan H.W., Shao Y., Li J.F., Mao W.L., Han Z.D., Shao C., Yao K.F., Phase stabilities of high entropy alloys. Scripta Materialia, 179, 40-44, 2020.

Mehranpour M.S., Shahmir H., Derakhshandeh A., Nili-Ahmadabadi M., Significance of Ti addition on precipitation in CoCrFeNiMn high-entropy alloy. Journal of Alloys and Compounds, 888, 161530, 2021.

Murty B.S., Yeh J.W., Ranganathan S., High-entropy alloys. Elsevier, 2014.

Otto F., Dlouhý A., Pradeep K.G., Kuběnová M., Raabe D., Eggeler G., George E.P., Decomposition of the single-phase high-entropy alloy CrMnFeCoNi after prolonged anneals at intermediate temperatures. Acta Materialia, 112, 40-52, 2016.

Otto F., Dlouhý A., Somsen C., Bei H., Eggeler G., George E.P. The influences of temperature and microstructure on the tensile properties of a CoCrFeMnNi high-entropy alloy. Acta Materialia, 61(15), 5743-5755, 2013.

Shahmir H., Mehranpour M.S., Shams S.A.A., Langdon T.G., Twenty years of the CoCrFeNiMn high-entropy alloy: Achieving exceptional mechanical properties through microstructure engineering. Journal of Materials Research and Technology, 23, 3362-3423, 2023.

Shun T.T., Chang L.Y., Shiu M.H., Microstructures and mechanical properties of multiprincipal component CoCrFeNiTix alloys. Materials Science and Engineering: A, 556, 170-174, 2012.

Tan C., Sun Q., Xiao L., Zhao, Y., Sun J., Slip transmission behavior across α/β interface and strength prediction with a modified rule of mixtures in TC21 titanium alloy. Journal of Alloys and Compounds, 724, 112-120, 2017.

Tan C., Sun Q., Zhang G., Role of microstructure in plastic deformation and crack propagation behaviour of an α/β titanium alloy. Vacuum, 183, 109848, 2021.

Xiaotao L., Wenbin L., Lijuan M., Jinling L., Jing L., Jianzhong C., Effect of boron on the microstructure, phase assemblage and wear properties of Al0. 5CoCrCuFeNi high-entropy alloy. Rare Metal Materials and Engineering, 45(9), 2201-2207, 2016.

Yang X., Zhang Y., Prediction of high-entropy stabilized solid-solution in multi-component alloys. Materials Chemistry and Physics, 132(2-3), 233-238, 2012.

Yeh J.W., Chen S.K., Lin S.J., Gan J.Y., Chin T.S., Shun T.T., Tsau C.H., Chang S.Y., Nanostructured high-entropy alloys with multiple principal elements: novel alloy design concepts and outcomes. Advanced engineering materials, 6(5), 299-303, 2004.

Yeh J.W., Recent progress in high entropy alloys. Annales De Chimie Science des Materiaux, 31(6), 633-648, 2006.

Zhang W., Liaw P.K., Zhang Y., Science and technology in high-entropy alloys. Sci. China Mater, 61(1), 2-22, 2018.

Zhang Y., Zuo T.T., Tang Z., Gao M.C., Dahmen K.A., Liaw P.K., Lu Z.P., Microstructures and properties of high-entropy alloys. Progress in materials science, 61, 1-93, 2014.

Zhou Y.J., Zhang Y., Wang Y.L., Chen G.L., Solid solution alloys of AlCoCrFeNiTix with excellent room-temperature mechanical properties. Applied physics letters, 90(18), 2007.

Zhou Y.J., Zhang Y., Wang Y.L., Chen, G.L., Microstructure and compressive properties of multicomponent Alx (TiVCrMnFeCoNiCu) 100− x high-entropy alloys. Materials Science and Engineering: A, 454, 260-265, 2007.